RSC Advances

ROYAL SOCIETY OF CHEMISTRY

www.rsc.org/advances

A sensitive dopamine biosensor based on ultra-thin polypyrrole nanosheets decorated with Pt nanoparticles

Hanieh Ghadimi*, M. R. Mahmoudian[a,c], Wan Jefrey Basirun*[a,b]

[a] Department of Chemistry, Faculty of Science, University of Malaya, 50603 Kuala Lumpur, Malaysia.

[b] Institute of Nanotechnology and Catalysis (NanoCat), University Malaya, Kuala Lumpur 50603, Malaysia.

[c] Department of Chemistry, Shahid Sherafat, University of Farhangian, 15916, Tehran, Iran.

Email addresses: Hanieh.Ghadimi@yahoo.com; M_R_mahmoudian@yahoo.com, jeff@um.edu.my

*Corresponding authors: Department of Chemistry, University of Malaya, Kuala Lumpur 50603, Malaysia. Tel: +60379675330; fax: +60379675330 Email addresses: jeff@um.edu.my Hanieh.Ghadimi@yahoo.com

Abstract

A sensitive and selective electrochemical sensor to determine dopamine (DA) was successfully fabricated from ultra-thin polypyrrole nanosheets (UltraPPy) that were decorated with Pt nanoparticles (Pt/UltraPPy–GCE). The morphology and structure of the modified electrode were characterized using transmission electron microscopy (TEM), atomic force microscopy (AFM), X-ray diffraction and Fourier-transformed infrared spectroscopy (FTIR). This new electrode displayed a synergistic effect of UltraPPy and Pt on the electro-oxidation of DA in the phosphate buffer solution at pH 7. The Pt/UltraPPy–GCE demonstrated excellent electrochemical activity towards DA oxidation compared with the bare GCE, UltraPPy–GCE and Pt NPs –GCE, possibly because of the larger surface area of the UltraPPy, which increased the interactions between the polymer and the K_2PtCl_4 solution during the Pt NPs deposition. The small size of the deposited Pt NPs resulted in a large surface area of Pt, which is suitable for the reaction with DA. Hence, Polypyrrole (PPy) in the nanocomposite material could crosslink to improve its stability with the Pt NPs. By applying the differential pulse voltammetry technique under optimized experimental conditions, a good linear ratio of oxidation peak currents and DA concentrations over a range of 0.01–400 μM was achieved with a limit of detection of 0.67 nM. This electrode was used to determine the DA concentration in DA hydrochloride injection.

1. Introduction

Dopamine (DA), which is one of the most significant catecholamines [1] in the mammalian central nervous system and biological organism, plays an important role in cardiovascular, drug addiction and Parkinson's disease, renal and hormonal systems. DA has also gathered the interest of neuroscientists and chemists because of its effects in attention span, cognition, emotions and neuronal plasticity [2]. DA coexists in high concentrations with other molecules in biological samples, which causes poor selectivity and sensitivity in DA determinations. Therefore, accurately measuring the DA concentrations in biological systems is important. Among various determination methods (such as mass spectrometry [3], fluorometry [4], radioenzymatic [5], electrochemistry [6], and chromatographic methods [7]), electrochemical methods have many inherent advantages such as economic, rapid response, sensitivity and easy miniaturization [8]. Hence, DA and other catecholamines are easily oxidized; therefore, their detection is possible using electrochemical methods [9]. Modified electrodes are the ideal candidate to solve this challenging bioanalytical problem because of their unique mechanical, chemical and physical properties [10].

Electrodes such as the MWCNT modified carbon paste electrode [11], thin pyrolytic carbon films [12], and Pt nanoparticles (NPs) supported on reduced graphene oxide [10] have been used for the sensitive electrochemical determination of DA. However, nanoscale conducting polymers have attracted considerable attention over the past few years in electronic devices, supercapacitors, functional electrodes, rechargeable batteries and sensors [13, 14] because of their good stability, reproducibility, increased active sites, homogeneity in electrochemical deposition and strong adherence to the electrode surface [15]. Recently, NPs of noble metal [16] have also attracted attention from the scientific and technological viewpoints because of their interesting

optical, photoelectrochemical, electrochemical and electronic properties [17, 18]. In recent years, there has been extensive research into the electrochemical studies of metal NP-modified electrodes [19, 20]. Previous studies indicate that Pt NPs can increase the surface area, are conducive to the electron transfer process with strong catalytic properties, and have attracted wide interests as materials for modified electrodes [21, 22].

Research efforts have also demonstrated that the synthesis of nanocomposites that contain both conducting polymers and NPs of noble metals such as silver, platinum and gold can be used as electrochemical sensors [23, 24]. Among the conductive polymers, PPy is one of the most promising conducting polymers because of its ease of preparation, wide range of applications, high electrical conductivity, good redox reversibility and high stability [25, 26]. The conductive properties of this polymer make it an important class of material for a wide range of applications such as chemical sensors [27, 28], biosensors [29], supercapacitors [30], gas sensors [31], corrosion protection [32] because of being environmentally stable, electrically conductive and flexible. Moreover, UltraPPy has a larger catalytic surface area because the entire surface of an UltraPPy acts as the active site. PPy has been successfully used as the conducting matrices of composite materials that incorporate Fe_3O_4, V_2O_5 and noble metals such as Au, Pd, Ag or Pt [33-36]. Recent reports show that the composite of polymers such as poly(nicotinamide) [37], polyethyleneimine [38] with noble metal nanoparticles are good candidates for the detection of DA. The present study demonstrates the synthesis of ultrathin polypyrrole nanosheets (UltraPPy) decorated with Pt NPs. The UltraPPy nanosheets were first prepared in the presence of sodium dodecyl sulfate (SDS) and deposited with Pt NPs on the surface of UltraPPy from an in situ reduction of K_2PtCl_4. To the best of our knowledge, there are no reports on the use of Pt/Ultra–thin–PPy–nanosheet–modified glassy carbon electrode (GCE) (Pt/UltraPPy–GCE) nanocomposite for the monitoring

of DA. The electrochemical behavior of DA at the Pt/UltraPPy–GCE was investigated using cyclic and differential pulse voltammetry. The stability, reproducibility and high range of detection are the important characteristics of the prepared biosensors, which coordinate the properties of UltraPPy and Pt NPs. A favorable electrode performance for DA detection is described in the following sections.

2. Experimental methods

2.1. Electrochemical apparatus

Electrochemical measurement, which involves the CV, differential pulse voltammetry (DPV) and chronoamperometry, were conducted using an Autolab potentiostat/galvanostat PGSTAT30 (Ecochemie Netherlands). A three-electrode system with a platinum wire as the auxiliary electrode and an Ag/AgCl (3 M NaCl) as a reference electrode was used in the electrochemical experiments. The working electrode was either the unmodified GCE or (Pt/UltraPPy–GCE). Unless otherwise stated, all potentials are quoted with respect to the reference electrode.

2.2. Materials

DA, distilled pyrrole, ascorbic acid, uric acid and potassium tetrachloroplatinate II (K_2PtCl_4) were purchased from Sigma Aldrich. All other chemicals (E Merck Germany) were of analytical grade and were used without further purification. The DA hydrochloride injection was purchased from the pharmacy center in University of Malaya hospital. Double-distilled water was used for all experimental procedures. A 0.1 M phosphate buffer (pH 7) was prepared by mixing the stock solutions of K_2HPO_4 and KH_2PO_4.

2.3. Synthesis of Pt–Ultra–thin PPy nanosheets

The Ultra-thin PPy was prepared similarly to the previous method in the literature [39, 40]. In summary, the chemical polymerization was performed by dissolving 2.45 g of SDS in 100 mL of distilled water in a reaction vessel; the reaction was maintained at 30 °C with continuous stirring at 800 rpm with a mechanical stirrer. Then, the solution was cooled to 0 °C. During this step, 20 mmol of the pyrrole monomer was added to this solution with continuous stirring for 30 min at 0 °C. A pre-cooled solution of 45 mmol ferric chloride (20 mL) was added drop-wise to the prepared mixture, and the white mixture gradually turned black. The stirring was continued for another 3 h at 0 °C for the complete polymerization of the UltraPPy. The resulting product was filtered, repeatedly washed with distilled water, and dried in a vacuum oven at 50 °C for 24 h.

The synthesized UltraPPy (0.05 g) was dispersed into 20 mL of distilled water with ultrasonication. This process was followed by the addition of 0.02 M K_2PtCl_4 to the dispersed UltraPPy solution with continuous stirring for 2 h at room temperature and the reduction by hydrazine hydrate at 50 °C for 1 h. The composite was subsequently filtered and repeatedly washed with distilled water, followed by drying in a vacuum oven at 60 °C for 24 h. The Pt NPs were prepared using the aforementioned procedure without the addition of UltraPPy.

2.4. Electrode preparation

The modified electrode was fabricated as follows: the GCE was polished with alumina, thoroughly rinsed with water/ethanol (V:V = 2:1), cleaned in an ultrasonic bath with water and finally rinsed with deionized water. Then, the cleaned GCE was dried at ambient temperature. The prepared Pt/UltraPPy (1 mg) was dispersed in 1 mL water for 1 h in an ultrasonic bath to

obtain a homogenous suspension. The Pt/UltraPPy suspension (15 µl) was drop-casted on the GCE surface and dried at 25 ± 5 °C to produce the Pt/UltraPPy–GCE electrode. The Pt/UltraPPy–GCE was subsequently used for further experiments.

2.5. Characterization methods

The phase and crystallite size of the Pt NPs were characterized using an automated X-ray powder diffractometer (XRD, PANalytical's Empyrean) with monochromated CuKα radiation (λ = 1.54056 Å). The particle size and structural characterization of the synthesized product were performed using a high-resolution transmission electron microscope (HRTEM-FEIG-4020, 500 kV). The samples were ultrasonicated in distilled water before the HRTEM characterization. Using an EDAX-System (Hitachi SU8000) instrument attached to the FESEM instrument, energy dispersive X-ray analysis (EDAX) was performed to investigate the elemental composition of the samples. An atomic force microscopy (AFM, PSIA XE-100) measurement was also used to analyze the surface morphology of the UltraPPy. The Fourier-transformed infrared (FTIR) analysis was performed on a Perkin Elmer System 2000 series spectrophotometer (USA) between 4000 and 450 cm^{-1}.

2.6. Procedure

The experiments were performed by studying the cyclic voltammetric behavior of the electrode in phosphate buffer (pH 7) as the supporting electrolyte at a potential range of -0.15–0.7 V and scan rates of 10-300 mV s^{-1}. The DPV was performed with potentials from -0.15 V to 1 V with a step potential of 2 mV, a modulation amplitude of 50 mV and a scan rate 10 mV s^{-1}. All experiments were conducted at 25±5 °C.

3. Results and discussions

3.1. Characterization of Pt/UltraPPy

3.1.1. Morphological and XRD analysis of the Pt/UltraPPy

The AFM scan and corresponding depth profiles in Fig. 1a confirm that the UltraPPy surface is flat. The thickness of the top and bottom layers of the UltraPPy, shown with an arrow (Fig. 1b), is ~ 40 nm, which confirms a nanosheet structure of the UltraPPy.

The TEM imaging technique was used for a detailed observation of the sample morphology (Figs. 1b, 1c and 1d). The TEM image (Fig. 1b) further support the AFM results (Fig. 1a). Fig. 1b shows that the UltraPPy is composed of two layers of UltraPPy, which are loosely held together as ultrathin nanosheets with a large surface area. Fig. 1c and 1d show that the nanosheets are decorated with Pt NPs. A lower magnification of TEM image in Fig. 1c clearly shows the surface coverage of UltraPPy by Pt, and indeed confirms the presence of a large amount of Pt NPs as dark spots embedded in the UltraPPy matrix. Moreover, the higher magnification of TEM image in Fig. 1d reveal that the Pt NPs are well distributed on the UltraPPy surface to form a nanocomposite structure, which can enhance the electrochemical detection of DA. Fig. 1e shows the histograms of the Pt nanoparticle diameter. The results also reveal that the Pt nanoparticle has a diameter of approximately 2.17 nm.

Furthermore, the EDX of the Pt/UltraPPy composite in Fig. 1f shows the existence of Pt (from the deposited nanoparticle), C and N (from PPy) and O from (SDS). The EDX result confirms that an appropriate percentage of Pt NPs deposition occurred on the UltraPPy surface. The weight percentage of each element is provided in Fig. 1f (inset).

The crystalline structure of Pt/UltraPPy was studied with XRD as shown in Fig. 1g. A broad amorphous diffraction peak in the range of 2Θ = 17-25° [39] is attributed to the scattering of

the interplanar spacing among the bare polymer chains [41]. In addition, the XRD profile of the sample shows three diffraction peaks at $2\Theta = 40.041$, 46.535 and 67.861°, which are attributed to the (111), (200) and (220) lattice planes of cubic Pt (JCPDS card no. 00-001-1194), respectively, with the lattice constant $a = b = c = 3.91$ Å. This result confirms that Pt^{2+} was reduced in the presence of the UltraPPy colloids.

<Fig. 1>

3.1.2. FTIR Spectroscopy

The FT-IR spectra of UltraPPy and Pt/UltraPPy display characteristic bands as shown in Fig. 2. In the FT-IR spectrum of the synthesized UltraPPy and Pt/UltraPPy, the peaks at 3325.42 and 3332.20 cm^{-1}, respectively, are attributed to the N-H bond [42]. The two absorption bands at 1185.33 cm^{-1} and 666.78 cm^{-1} are assigned to the SO_3 stretch (and S-O stretch), which occurs because the UltraPPy is synthesized in the presence of SDS. In addition, the identical characteristic bands for SO_3 and S-O are observed in the FT-IR spectrum of Pt/UltraPPy (Fig. 2(b)), but with a slight shift in wavenumbers. The slight shift in wavenumbers of SO_3 at 1186.05 cm^{-1} and S-O at 667.70 cm^{-1} in the FT-IR spectrum of the Pt/UltraPPy compared with UltraPPy can account for the interaction between Pt and the non-bonding electron pair, similar to that from O (from SDS). The peaks at 1708.63 cm^{-1} (Fig. 2(a)) and 1710.25 cm^{-1} (Fig. 2(b)) are related to the C-N-C bond vibrations in the UltraPPy and Pt/UltraPPy spectra, respectively [43]. The band at 2847.45 cm^{-1} (Fig. 2(a)) and the strong band at 2850.84 cm^{-1} (Fig. 2(b)) are associated with the aliphatic C-H vibrations, which also confirms that an appropriate percentage of Pt NPs was deposited on the UltraPPy surface. The bands at 1425.47 cm^{-1} and 1461.31 cm^{-1} are assigned to the typical PPy ring vibrations.

<Fig. 2>

3.2. EIS studies

EIS is a widely used technique to study modified electrodes to obtain deeper understanding of the electron transfer process across the electrode/electrolyte interface. The EIS experiment was performed on the bare GCE, UltraPPy–GCE, Pt NPs–GCE and Pt/UltraPPy–GCE. Fig. 3A shows the Nyquist plots in 0.1 M KCl solution with 1 mM $[Fe(CN)_6]^{3-/4-}$ (1:1) in a frequency range of 0.1-10^5 Hz at the formal potential of the redox probe (5 mV).

The Nyquist plot of the impedance spectra consists of a semicircle portion in a higher-frequency region, which is attributed to the electron transfer limiting process, whereas a linear portion at the lower-frequency region is attributed to a diffusion limiting process. The Pt/UltraPPy–GCE (curve a) demonstrates a much lower charge transfer resistance than the Pt NPs–GCE (curve b), UltraPPy–GCE (curve c) and bare GCE (curve d).

The electron transfer resistance (R_{ct}) is evaluated from the semicircle diameter (see Supporting information Table. S1). To clearly realize the electron transfer behavior across the electrode/electrolyte interface, the Randles' equivalent circuit of $R_s(Q[R_{ct}W])$ accurately fits the experimental data (Fig. 3B) with a minimized chi square (χ^2) value of 10^{-3}. In this circuit, R_s represents the solution resistance, CPE is the constant phase element, which is an approximation of the double-layer capacitance, and R_{ct} is the resistance against the electron transfer process, which is parallel to the CPE. In addition, the Warburg element, which represents the diffusion impedance, is in series with R_{ct}. From the simulation of the experimental results, R_{ct} increases in the order of Pt/UltraPPy–GCE (476.02 Ω) < Pt NPs–GCE (936.87 Ω) < UltraPPy–GCE (2236.5 Ω) < GCE (7517.4 Ω). The CV and EIS simulation results show that the electron transfer process

can be improved with the presence of Pt in the nanocomposite-modified electrode (Pt/UltraPPy–GCE) compared with the other modified electrodes. Therefore, it is concluded that the Pt/UltraPPy–GCE nanocomposite benefits from the synergistic effect of Pt and UltraPPy, and UltraPPy is an electron mediator in the electron transfer process.

<Fig. 3>

3.3. Electrochemistry behavior of DA

The performance of the Pt/UltraPPy–GCE was investigated using cyclic voltammetry in 0.1 M phosphate buffer solutions (pH 7) in the presence of 100 μM DA. The broad redox couple peaks of DA at the bare GCE, UltraPPy–GCE and Pt NPs–GCE (Figs. 4a, 4b and 4c) indicate a slow electron transfer process. The UltraPPy–GCE (Fig. 4b) has a largest peak current than the bare GCE because of the over-oxidation phenomena, which can occur for PPy during the oxidation of DA and causes the direct oxidation of DA in the presence of PPy. The high surface area of UltraPPy increases the interaction with Pt^{2+} ions and direct oxidation of DA by PPy. The peak current improvement is more noticeable on the surface of Pt NPs–GCE (Fig. 4c) compared with the bare GCE and UltraPPy–GCE because Pt has superior catalytic activity for DA oxidation.

A larger peak current response for the electrochemical oxidation of DA was obtained at the Pt/UltraPPy–GCE (Fig. 4d). It is observed that the Pt/UltraPPy–GCE has a considerable effect with approximately 5 times improvement in peak current compared to the UltraPPy–GCE. The Pt/UltraPPy–GCE has obviously largest peak current than the UltraPPy–GCE because there are Pt NPs on the UltraPPy. The UltraPPy morphology can create a large surface area for Pt^{2+} to interact with the polymer nanosheets during the Pt NPs deposition. The lower electrical

conductivity of the UltraPPy can be improved with the presence of Pt NPs, which together act synergistically for the DA oxidation. The TEM results (Figs. 1c and 1d) show a large amount of deposited Pt nanoparticles on the surface of the UltraPPy; thus, it can produce a large catalytic current on the Pt/UltraPPy–GCE.

<Fig. 4>

3.4. Effects of the pH solution

The effect of pH on the electrochemical response of the Pt/UltraPPy–GCE towards the addition of 100 μM DA was investigated using CV. The change in peak current with pH (pH range of 4–7.8) is shown in Fig. S1A (Supporting information). It is observed that I_{pa} increases with pH until pH 7. However, in Fig. 4, I_{pa} of DA in the phosphate buffer (pH 7) is higher than the reduction peak current I_{pc}, which indicates a quasi-reversible electrode process. Consequently, the buffering at pH 7, which is near the physiological pH, is used for the remainder of the work. Smaller currents were detected when the pH value of the solution was either lower or higher than 7. The effect of the phosphate buffer pH on E_{pa} was investigated, and the results show that E_{pa} was shifted toward negative potentials with a slope of -58 mV decade^{-1}. A linear relationship of E_{pa} (mV) = -58.9 pH + 657.1 was obtained with (R^2= 0.997) Fig. S1B (supporting information). The slope is notably close to the Nernstian value of -59 mV decade^{-1}, which suggests that the numbers of protons and electrons transferred in the redox reaction of DA are equal [1, 44-46]. Two electrons and two protons are involved for the oxidation of DA. Thus, the mechanism of the redox process of DA is proposed in Scheme 1 [47] (supporting information).

3.5. Effects of scan rate

The scan rate dependency of the modified electrode in 100 μM DA was also investigated (Fig. 5). The redox peak current of the Pt/UltraPPy–GCE in the DA solution increases linearly with the increase of the scan rate from 10 to 300 mV s^{-1}. In addition, E_{pa} is slightly shifted to the positive region, whereas E_{pc} is shifted to the negative region possibly because of the changes in electrocatalytic activity and kinetic effect of the Pt/UltraPPy–GCE surface towards the DA oxidation, particularly at scan rates higher than 100 mV s^{-1}. In other words, at scan rates greater than 100 mV s^{-1}, the DA oxidation becomes relatively slower because of the short timescales, which decreases the facile electron transfer process. The linear relationship between the peak current and the scan rate is expressed using the following linear regression equation: $I_{pa}/\mu A = 3.39X + 107.38\ v/\text{mV s}^{-1}$ ($R^2 = 0.994$) and $I_{pc}/\mu A = -3.75X - 103.99\ v/\text{mV s}^{-1}$ ($R^2 = 0.995$). These results indicate that the electrochemical reaction of DA on the Pt/UltraPPy–GCE is a surface-controlled process [48, 49].

<Fig. 5>

3.6. Determination of DA using differential pulse voltammetry

Figure 6 shows the differential pulse voltammogram (DPV) of different concentrations of DA in 0.1 M phosphate buffer (pH 7) between -0.15-1 V with a step potential of 2.0 mV, a modulation amplitude of 50 mV and a scan rate of 10 mV s^{-1}. I_{pa} is linearly proportional to the DA concentration in the range of 0.01–400 μM. A linear equation of I_{pa} (μA) = 0.9239 [DA] (μM) + 29.292 with (R^2 = 0.998) was obtained (Fig. 6). The detection limit of DA at Pt/UltraPPy–GCE is 0.67 nM. Table 1 shows a comparison between the result of this work and

other results for the DA determination. The limit of detection of DA at the Pt/UltraPPy–GCE shows better sensitivity than those in previous reports.

<Fig. 6>

<Table 1>

3.7. Interference effects

Ascorbic acid (AA) and uric acid (UA) are common compounds found with DA in real samples such as biological fluids. Because the oxidation potentials of these three compounds are always close, the overlap of the oxidation peaks and interferences from the other two compounds are major problems that are encountered in DA detection. Therefore, the effects of AA and UA on the DA measurement were investigated using the amperometric response of successive additions of 100 μM DA and 100 μM of AA and UA in a phosphate buffer solution (pH 7.0) at 200 mV (Fig. 7a). However, the result demonstrates that the presence of AA and UA does not affect the DA response. Nonetheless, when 100 μM DA is spiked into the phosphate buffer solution with AA and UA, I_{pa} sharply increases. The results indicate that the Pt/UltraPPy–GCE has high selectivity towards DA detection even in the presence of some common interfering compounds that are normally found in biological samples.

The effects of AA and UA on the DA measurement were investigated on Pt/UltraPPy–GCE using DPV method as well. The electrooxidation processes of DA, AA and UA in the mixture are evaluated when the concentration of one species is changed and the other two are kept constant. Figure 7b illustrates the DPV curves of various DA concentrations at Pt/UltraPPy–GCE in the presence of 100 μM UA and 100 μM AA. The results indicate that the peak current response for the oxidation of DA increases linearly with the increase of the DA concentration in

the range 0.01-400 μM, while the peak current for AA and UA oxidation is almost unchanged. The result obtained is similar with a previous study on the effects of AA and UA on the DA determination [10, 44]. These results confirm that there are no significant interferences for the detection of DA in the presence of AA and UA.

<Fig. 7>

3.8. Analysis of the real samples

3.8.1. DA determination in DA hydrochloride injection

To evaluate the validity of the method to analyze DA in pharmaceutical products, the Pt/UltraPPy–GCE was further tested for the DA measurement in DA hydrochloride injection (concentration of DA 10 mg mL^{-1}, 2 mL per injection). The injection solution was diluted to 50 mL with distilled water. Then, 100 μL of this solution was transferred to 50 mL volumetric flasks and diluted with 0.1 M phosphate buffer (pH 7). A portion of the resulting solution (5 mL) was subsequently removed to be the sample for the DA determination using DPV. The recovery was obtained by using DPV to evaluate the method accuracy. Based on the replicates (n=5), the relative standard deviation of this method is presented in Table S2 (Supporting information). Satisfactory recoveries of DA at Pt/UltraPPy–GCE in the range of 0.01-400 μM show that this method is effective and reliable. These findings indicate that this method is rapid and simple for the selective and sensitive analysis of DA in pharmaceutical preparations.

3.9. Reproducibility and stability of Pt/UltraPPy–GCE

The electrode reproducibility was examined using cyclic voltammetry studies of seven electrodes, which were constructed with the same procedure in seven DA samples. The relative

standard deviation (RSD) of I_{pa} is 3.43 % (n=7), which indicates good reproducibility. In addition, the operational and storage stabilities of the Pt/UltraPPy–GCE to oxidize 100 μM DA in both synthetic and real samples were also studied. Long-term stability is obtained when the modified electrode is maintained in 0.1 M phosphate buffer (pH 7) at 4 °C when not in use. The operational stability is retained at 99 % of the initial current when it was constantly used for two months.

4. Conclusion

A new electrode based on Pt/UltraPPy–GCE was prepared and investigated using various characterization methods such as FT-IR, XRD, TEM and AFM. The results confirm that the Pt NPs were deposited on the UltraPPy surface. The electrode displays higher electrocatalytic activity toward the DA oxidation than the GCE, UltraPPy–GCE and Pt NPs–GCE. The incorporation of Pt into the UltraPPy composite significantly increases the conductivity and effective electroactive surface area of the electrode. The ultra PPy provides a larger surface area to deposit Pt^{2+} NPs, where Pt^{2+} NPs can provide a suitable surface area for the electrocatalytic reaction of DA. Additionally, the Pt/UltraPPy–GCE exhibits a low detection limit for DA oxidation with improvement in the anodic peak current. The electrode is not interfered by common physiological interferences such as AA and UA. The proposed sensor was successfully applied to determine DA in a DA hydrochloride injection with good precision and accuracy.

Acknowledgements

The authors would like to thank University of Malaya and Ministry of Higher Education for providing financial assistance under grant numbers of FP033 2013A and GC001C-14SBS.

References

1. X. Kan, H. Zhou, C. Li, A. Zhu, Z. Xing and Z. Zhao, *Electrochim Acta*, 2012, **63**, 69-75.
2. W. Sun, X. Wang, Y. Wang, X. Ju, L. Xu, G. Li and Z. Sun, *Electrochim. Acta*, 2013, **87**, 317-322.
3. M. J. Whiting, *Ann. Clin. Biochem.* , 2009, **46**, 129-136.
4. H.-P. Wu, T.-L. Cheng and W.-L. Tseng, *Langmuir*, 2007, **23**, 7880-7885.
5. D. L. Hard, R. K. Bhatnagar, J. R. Molina and L. L. Anderson, *Domest. Anim. Endocrinol.*, 2001, **20**, 89-100.
6. Y. Wang, J. Kang, H. Wu, Z. Xue and X. Lu, *Anal. Lett.* , 2005, **37**, 575-590.
7. M. C. Jung, G. Shi, L. Borland, A. C. Michael and S. G. Weber, *Anal. Chem.*, 2006, **78**, 1755-1760.
8. U. Yogeswaran and S.-M. Chen, *Electrochim. Acta.*, 2007, **52**, 5985-5996.
9. C.-F. Tang, S. A. Kumar and S.-M. Chen, *Anal. Biochem.* , 2008, **380**, 174-183.
10. T.-Q. Xu, Q.-L. Zhang, J.-N. Zheng, Z.-Y. Lv, J. Wei, A.-J. Wang and J.-J. Feng, *Electrochim. Acta.*, 2014, **115**, 109-115.
11. H. Beitollahi, A. Mohadesi, S. K. Mahani, H. Karimi-Maleh and A. Akbari, *Turk. J. Chem.*, 2012, **36**, 526-536.
12. G. P. Keeley, N. Mcevoy, H. Nolan, S. Kumar, E. Rezvani, M. Holzinger, S. Cosnier and G. S. Duesberg, *Anal. Methods*, 2012, **4**, 2048-2053.
13. C. Bora and S. K. Dolui, *Polymer*, 2012, **53**, 923-932.
14. H. Kim, A. A. Abdala and C. W. Macosko, *Macromolecules*, 2010, **43**, 6515-6530.
15. G. Jin, F. Huang, W. Li, S. Yu, S. Zhang and J. Kong, *Talanta*, 2008, **74**, 815-820.

16. J. Wang, *Microchim. Acta*, 2012, **177**, 245-270.

17. M. A. Zavareh, A. A. D. M. Sarhan, B. B. A. Razak and W. J. Basirun, *Ceram. Int.*, 2014, **40**, 14267-14277.

18. M. Akhtari Zavareh, A. A. D. M. Sarhan, B. B. Razak and W. J. Basirun, *Ceram. Int.*, 2015.

19. H.-J. Qiu, G.-P. Zhou, G.-L. Ji, Y. Zhang, X.-R. Huang and Y. Ding, *Colloids Surf., B*, 2009, **69**, 105-108.

20. G.-Z. Hu, D.-P. Zhang, W.-L. Wu and Z.-S. Yang, *Colloids Surf., B*, 2008, **62**, 199-205.

21. S. Hrapovic, Y. Liu, K. B. Male and J. H. T. Luong, *Anal. Chem.*, 2003, **76**, 1083-1088.

22. P. R. Birkin, J. M. Elliott and Y. E. Watson, *Chem. Commun.*, 2000, 1693-1694.

23. Y. Fan, J.-H. Liu, C.-P. Yang, M. Yu and P. Liu, *Sens. Actuators, B* 2011, **157**, 669-674.

24. Y. Luo, W. Lu, G. Chang, F. Liao and X. Sun, *Electrochim. Acta*, 2011, **56**, 8371-8374.

25. Q.-F. Wu, K.-X. He, H.-Y. Mi and X.-G. Zhang, *Mater. Chem. Phys.* , 2007, **101**, 367-371.

26. C. Zhou, S. Kumar, C. D. Doyle and J. M. Tour, *Chem. Mater.*, 2005, **17**, 1997-2002.

27. H. Qin, A. Kulkarni, H. Zhang, H. Kim, D. Jiang and T. Kim, *Sens. Actuators, B*, 2011, **158**, 223-228.

28. P. Moozarm Nia, F. Lorestani, W. P. Meng and Y. Alias, *Appl. Surf. Sci.*, **332**, 648-656.

29. P. Moozarm Nia, W. P. Meng, F. Lorestani, M. R. Mahmoudian and Y. Alias, *Sens. Actuators, B*, 2015, **209**, 100-108.

30. Y. Liu, Y. Zhang, G. Ma, Z. Wang, K. Liu and H. Liu, *Electrochim. Acta.*, 2013, **88**, 519-525.

31. Y. Mao, Q. Kong, B. Guo, X. Fang, X. Guo, L. Shen, M. Armand, Z. Wang and L. Chen, *Energy Environ. Sci.*, 2011, **4**, 3442-3447.

32. R. Vera, R. Schrebler, P. Grez and H. Romero, *Prog. Org. Coat.*, 2014, **77**, 853-858.

33. Shy Chyi Wuang, Koon Gee Neoh, En-Tang Kang, Daniel W. Pack and D. E. Leckbandb, *J. Mater. Chem.*, 2007, **17**, 3354-3362.

34. Y.-C. Liu and T. C. Chuang, *J. Phys. Chem. B*, 2003, **107**, 12383-12386.

35. M. Sigaud, M. Li, S. Chardon-Noblat, F. J. C. S. Aires, Y. Soldo-Olivier, J. P. Simon, A. Renouprez and A. Deronzier, *J. Mater. Chem.*, 2004, **14**, 2606-2608.

36. M. Ferreira, V. Zucolotto, F. Huguenin, R. M. Torresi and O. N. Oliveira, *J. Nanosci. Nanotechnol.*, 2002, **2**, 29-32.

37. B. Li, Y. Zhou, W. Wu, M. Liu, S. Mei, Y. Zhou and T. Jing, *Biosens. Bioelectron.*, 2014, **67**, 121-128.

38. V. K. , V. Mani, S.-M. Chen, W.-T. Huang and J.-F. Jen, *Talanta*, 2014, **120**, 148-157.

39. M. R. Mahmoudian, Y. Alias, W. J. Basirun and M. Ebadi, *Electrochim. Acta*, 2012, **72**, 46-52.

40. S. S. Jeon, H. H. An, C. S. Yoon and S. S. Im, *Polymer*, 2011, **52**, 652-657.

41. I. Seo, M. Pyo and G. Cho, *Langmuir*, 2002, **18**, 7253-7257.

42. P. Crews, 1998. Organic Structure Analysis. Newyork, Oxford: P. 63,331,332, 333,336.

43. P. Y. Bruice, 2004. Organic Chemistry. United States: 2nd Edition, Pearson Education Inc.

44. J. Du, R. Yue, F. Ren, Z. Yao, F. Jiang, P. Yang and Y. Du, *Gold Bull*, 2013, **46**, 137-144.

45. W. Cai, T. Lai, H. Du and J. Ye, *Sens. Actuators, B*, 2014, **193**, 492-500.

46. X. Wang, N. Yang, Q. Wan and X. Wang, *Sens. Actuators, B*, 2007, **128**, 83-90.

47. A. J. Bard and L. R. Faulkner.

48. S. Cheemalapati, S. Palanisamy, V. Mani and S.-M. Chen, *Talanta*, 2013, **117**, 297-304.

49. S. A. Kumar, C.-F. Tang and S.-M. Chen, *Talanta*, 2008, **74**, 860-866.

50. D. Jia, J. Dai, H. Yuan, L. Lei and D. Xiao, *Talanta*, 2011, **85**, 2344-2351.

51. L. Yang, D. Liu, J. Huang and T. You, *Sens. Actuators, B*, 2014, **193**, 166-172.

52. Y.-R. Kim, S. Bong, Y.-J. Kang, Y. Yang, R. K. Mahajan, J. S. Kim and H. Kim, *Biosens. Bioelectron.* , 2010, **25**, 2366-2369.

53. P. Wang, Y. Li, X. Huang and L. Wang, *Talanta*, 2007, **73**, 431-437.

54. M. Noroozifar, M. Khorasani-Motlagh and A. Taheri, *Talanta*, 2010, **80**, 1657-1664.

55. J. Du, R. Yue, F. Ren, Z. Yao, F. Jiang, P. Yang and Y. Du, *Biosens. Bioelectron.*, 2014, **53**, 220-224.

56. M. Zhong, Y. Teng, S. Pang, L. Yan and X. Kan, *Biosens. Bioelectron.*, 2015, **64**, 212-218.

57. Q. Huang, H. Zhang, S. Hu, F. Li, W. Weng, J. Chen, Q. Wang, Y. He, W. Zhang and X. Bao, *Biosens. Bioelectron.*, 2014, **52**, 277-280.

58. R. Suresh, K. Giribabu, R. Manigandan, S. P. Kumar, S. Munusamy, S. Muthamizh, A. Stephen and V. Narayanan, *Sens. Actuators, B*, 2014, **202**, 440-447.

Figures and Table Captions

Figure 1. (a) AFM image and the corresponding depth profile of UltraPPy; TEM images of (b) UltraPPy, UltraPPy deposited with Pt NPs in (c) low magnification and (d) high magnification; (e) size distribution diagram of the Pt/UltraPPy composite;, respectively (f) EDX of UltraPPy deposited with Pt NPs; (g) XRD pattern of UltraPPy deposited with Pt NPs.

Figure 2. FT-IR of (a) UltraPPy synthesized in the presence of SDS and (b) UltraPPy deposited with Pt NPs.

Figure 3. (A) Nyquist Plots of: (a) Pt/UltraPPy–GCE, (b) Pt NPs–GCE, (c) UltraPPy–GCE and (d) bare GCE in 1 mM $Fe(CN)_6^{3-/4-}$ (1:1) solution with 0.1 M KCL supporting electrolyte.

(B) Equivalent circuit for the system.

Figure 4. CVs of 100 μM DA in 0.1 M phosphate buffer solution (pH 7.4) at the scan rate of 20 mV s^{-1} at (a) bare GCE, (b) UltraPPy–GCE, (c) Pt NPs–GCE and (d) Pt/UltraPPy–GCE.

Figure 5. (A) CVs of 100 μM DA in 0.1 M phosphate buffer (pH 7.4) at Pt/UltraPPy–GCE at scan rates 10, 20, 30, 40, 50, 100, 200, 300 mV s^{-1}; (B) Linear relationship of I_{pa} and I_{pc} for 100 μM DA vs. scan rate.

Figure 6. DPVs of 0.01, 2, 10, 25, 50, 75, 125, 150, 175, 210, 250, 300 and 400 μM DA in phosphate buffer (pH 7) at Pt/UltraPPy–GCE.

Figure 7. (a) Amperometric response of Pt/UltraPPy–GCE towards the interference in phosphate buffer (pH 7) at 200 mV with successive additions of 100 μM DA, AA and UA as indicated. (b) DPV of Pt/UltraPPy–GCE in 0.1 M phosphate buffer (pH 7) containing 100 μM AA and UA in the presence of different concentration of DA: 0.01, 5, 10, 50, 125, 250, 300, 400; Inset b_1 DPV curve of AA in the presence of DA. Inset b_2 Plot of oxidation currents versus the concentration of DA.

Table 1 Electrochemical response of some DA sensors constructed from various materials.

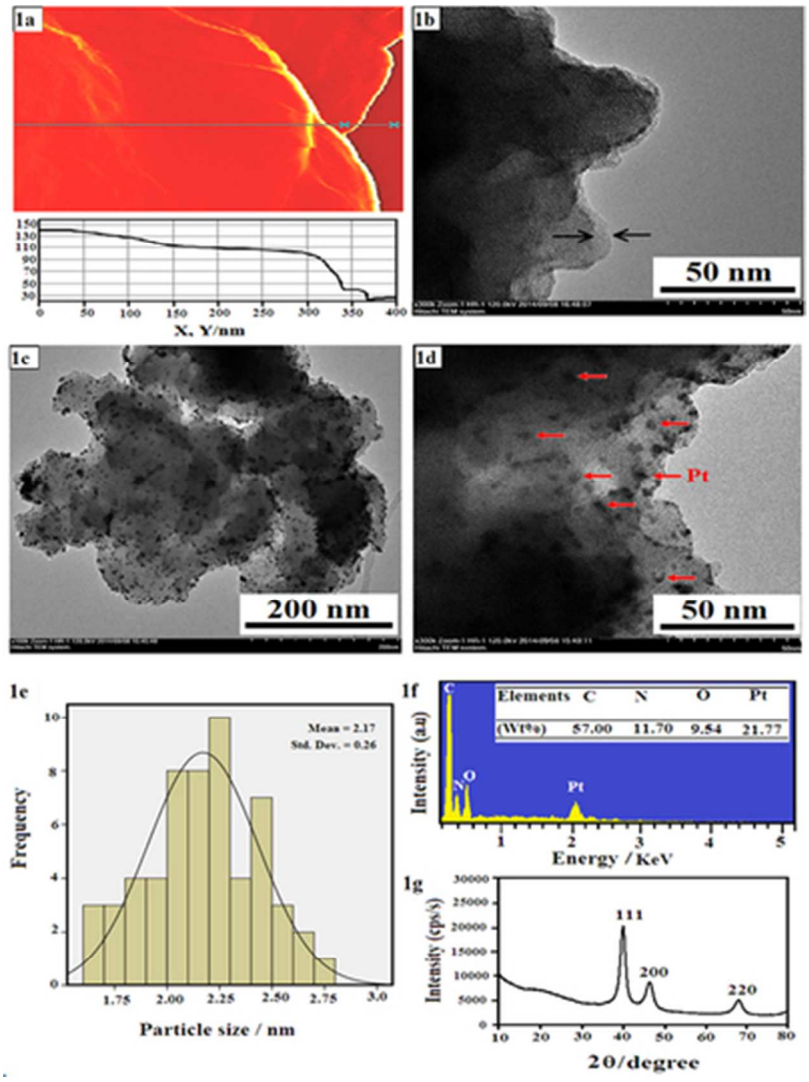

33x45mm (300 x 300 DPI)

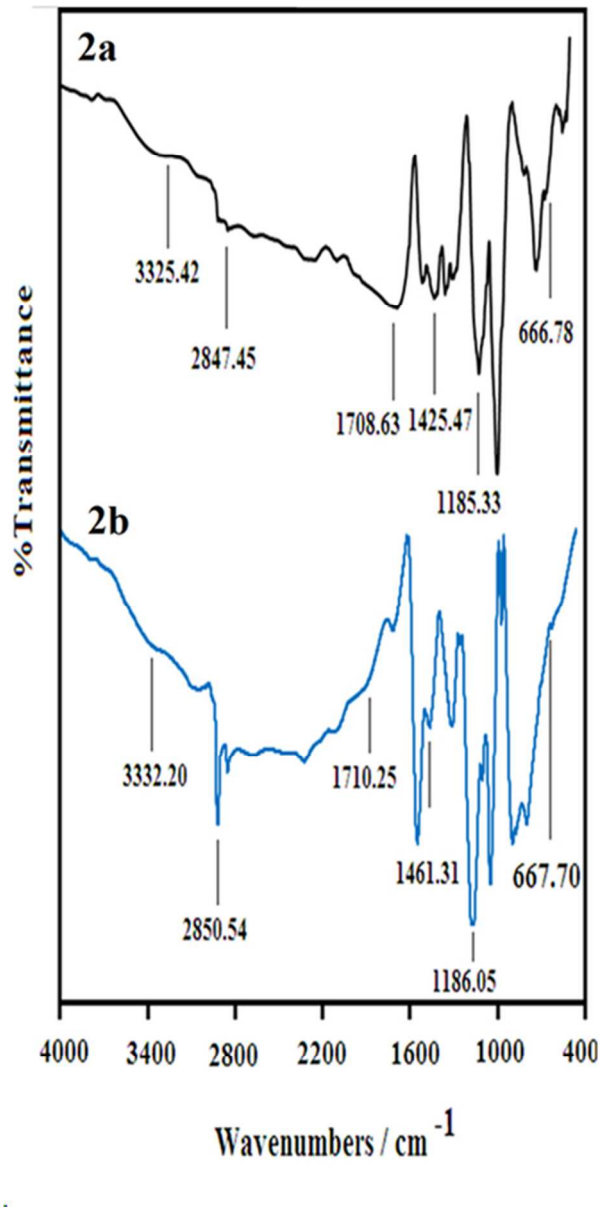

39x74mm (300 x 300 DPI)

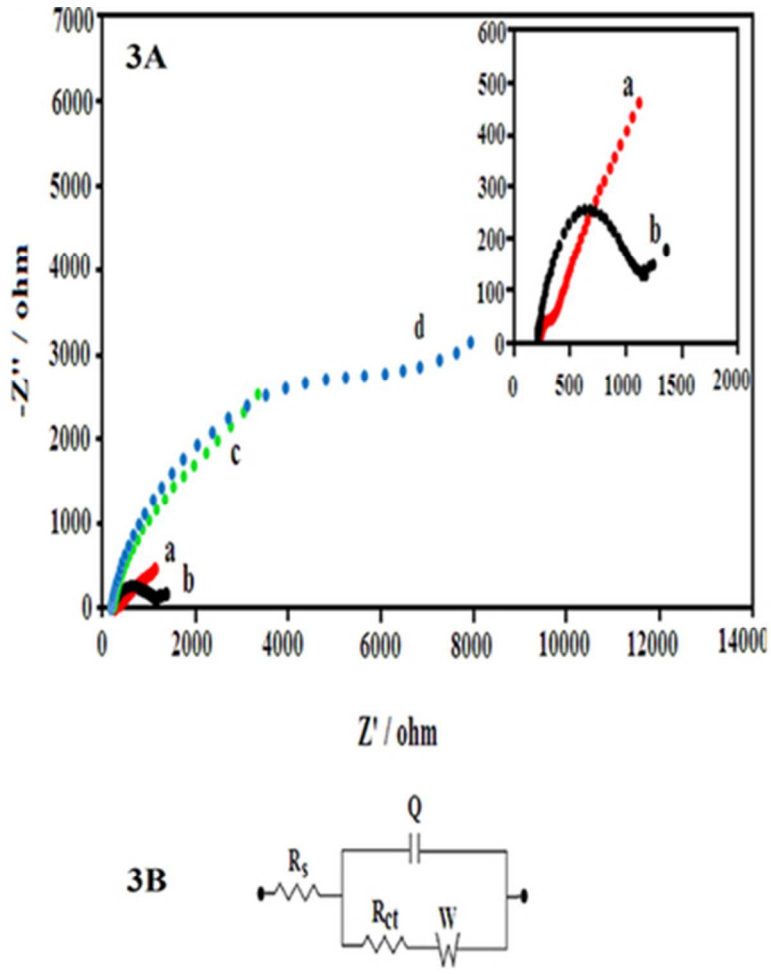

32x41mm (300 x 300 DPI)

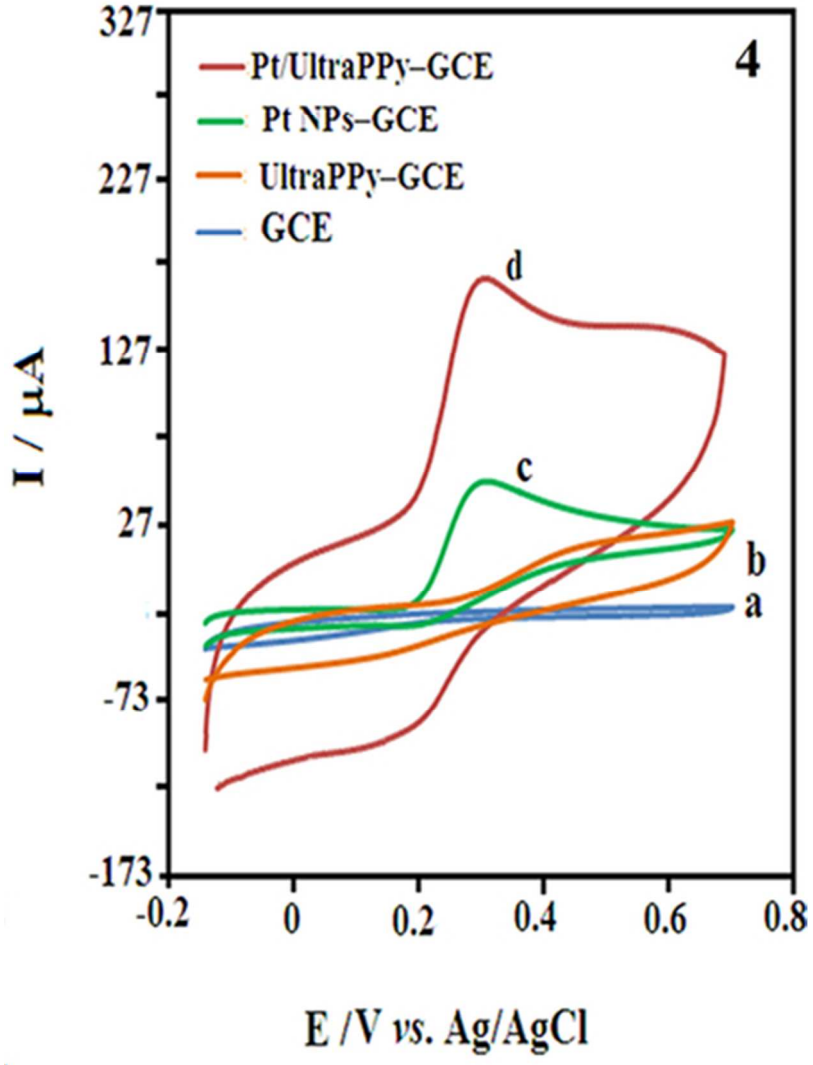

33x45mm (300 x 300 DPI)

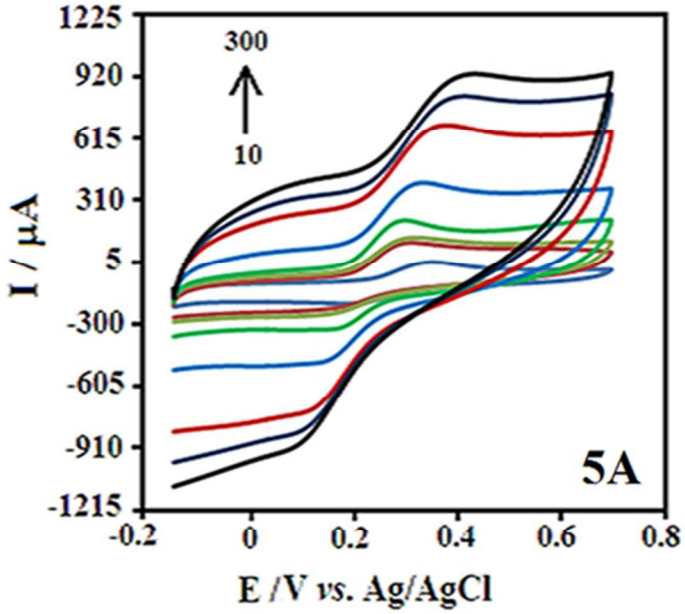

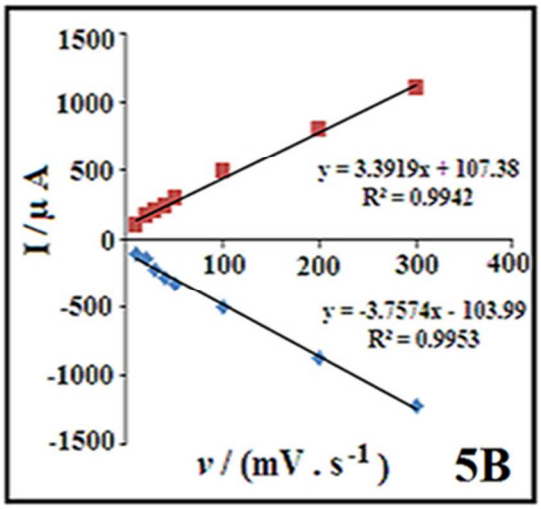

39x64mm (300 x 300 DPI)

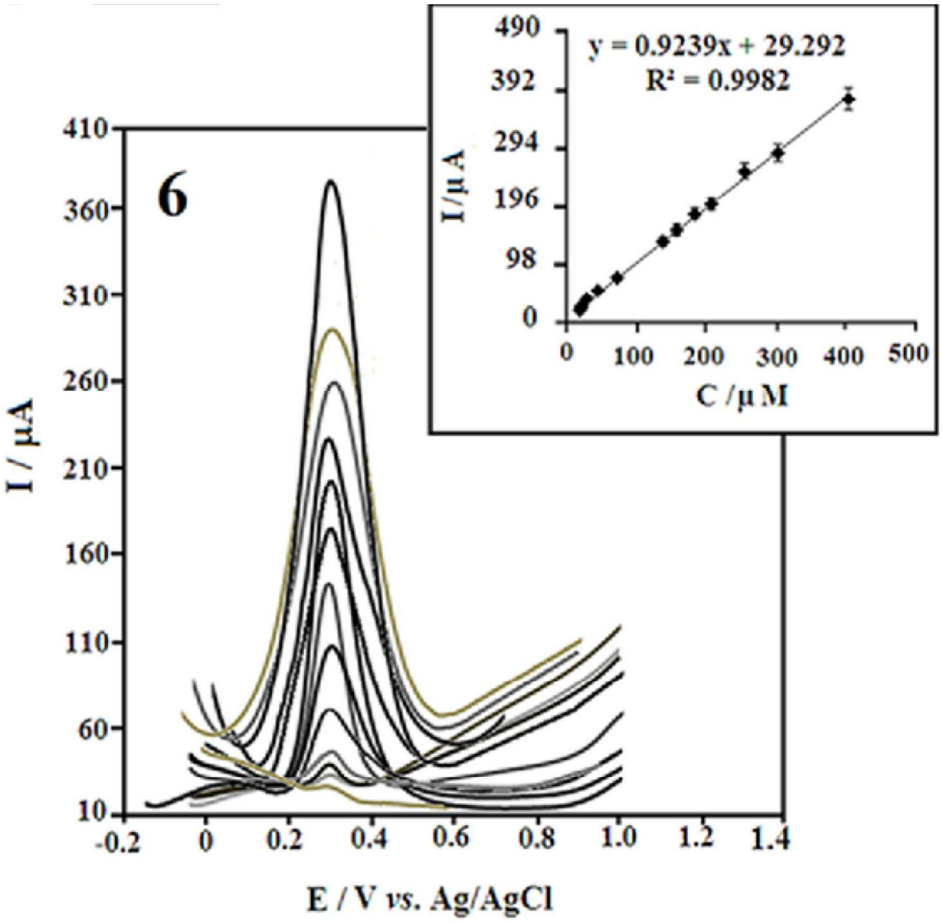

97x94mm (300 x 300 DPI)

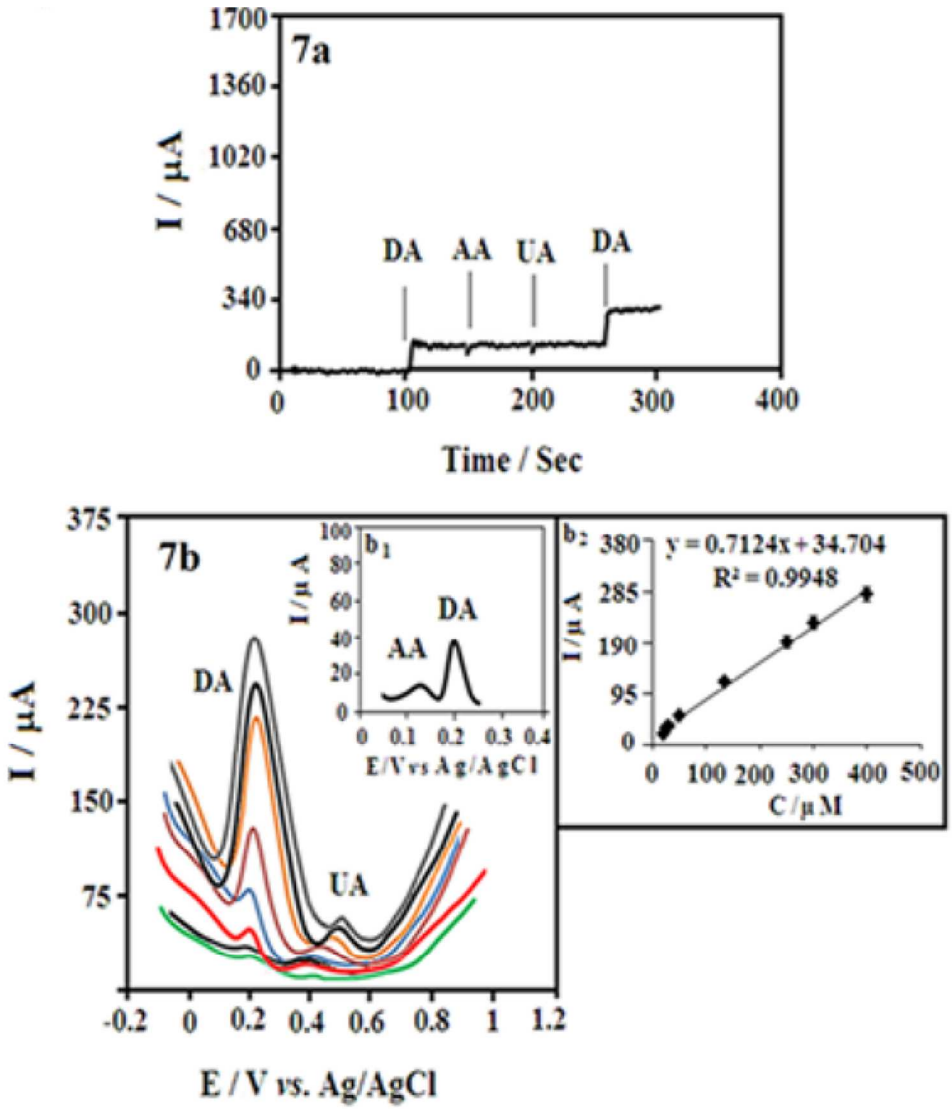

116x134mm (300 x 300 DPI)

Table 1

Electrode materials	Technique	Detection limit	Linear range (µM)	Ref.
Multiwall carbon nanotubes/5- amino-3',4'-dimethoxy-biphenyl-2- ol modified carbon paste electrode	Square Wave Voltammetry	0.16 µM	1.2-800	11
ß-CD-MWCNTs/Plu-AuNPs/GCE	Amperometry	0.19 µM	1-56	50
Pt-reduced graphene/GCE	DPV	0.25 µM	10-170	10
Electrochemically reduced graphene oxide	DPV	0.5 µM	0.5-60	51
Graphene modified electrode	DPV	2.64 µM	4-100	52
Gold nanoparticle choline/GCE	DPV	0.12 µM	0.2-80	53
GC/CNT-Silver hexacyanoferrate nanoparticles modified electrode	CV	0.14 µM	2.4-130	54
Molecular imprinted polymer/MWCN/GCE	DPV	0.06 µM	0.6-100	1
Graphene flowers modified carbon fiber	DPV	0.5 µM	0.7-45.21	55
Graphene nanosheets/ polyethyleneimine/Gold nanoparticle	DPV	0.2 µM	2-48	38
MIP/GCE	DPV	0.033 µM	0.05-10	56
Au@carbondots–chitosan modified GCE	DPV	0.001 µM	0.01-100	57
Ni-doped V_2O_5 nanoplates modified GCE	Chronoamperometric	28 nM	6.6-96.4	58
Exfoliated graphite paper electrode	DPV	0.01 µM	0.5-35	45
Pt/UltraPPy–GCE	DPV	0.67 nM	0.01–400	This work